Changing source characteristics during multifragment decay

T. M. Hamilton, E. Cornell, D. Fox,* Y. Lou, and R. T. de Souza
Department of Chemistry and Indiana University Cyclotron Facility, Indiana University, Bloomington, Indiana 47405

M. J. Huang, W. C. Hsi,† C. Schwarz,‡ C. Williams, D. R. Bowman,* J. Dinius, C. K. Gelbke, T. Glasmacher, D. O. Handzy,§ M. A. Lisa,‖ W. G. Lynch, G. F. Peaslee,¶ L. Phair,‖ and M. B. Tsang
National Superconducting Cyclotron Laboratory and Department of Physics and Astronomy, Michigan State University, East Lansing, Michigan 48824

G. VanBuren,** R. J. Charity, and L. G. Sobotka
Department of Chemistry, Washington University, St. Louis, Missouri 63130

A. A. Sonzogni and D. Prindle
Department of Chemistry and Nuclear Physics Laboratory, University of Washington, Seattle, Washington
(Received 13 October 1995)

The spatial-temporal extent of the emitting system for central collisions in $^{84}Kr + {}^{197}Au$ at $E/A = 35$, 55, and 70 MeV is probed using fragment-fragment velocity correlation functions. Selection on fragment pairs of high velocity yields a stronger fragment-fragment Coulomb interaction than for inclusive fragment pairs. This result is consistent with fragment emission from a source of decreased spatial-temporal extent. The universality of this association and the effect of different selection criteria are explored. The sensitivity of the spatial-temporal extent deduced by the correlation function technique to measurement uncertainties, assumed source characteristics, and rotational effects is assessed. [S0556-2813(96)05905-5]

PACS number(s): 25.70.Pq

I. INTRODUCTION

Collisions of intermediate energy heavy ions can result in the formation of transient nuclear systems of considerable excitation and angular momentum [1–11]. Whether such reactions probe the spinodal region of the nuclear temperature-density plane is presently a topic of considerable debate [12–14]. Evidence for the spinodal decomposition of low density nuclear matter is suggested by multifragment decay of the excited composite system [12,15–19]. Much experimental and theoretical attention has been focused on elucidating the essential character of this novel decay mode [20,21].

While the recent attempts focusing on the scaling and reducible nature of multifragmentation [7,22,23] are surprisingly successful, such attempts ignore the temporal nature [11,13,24,25] of the multifragmentation process. If fragments are emitted sequentially during the deexcitation of the source, then earlier emissions should manifest a shorter time between emissions due to the higher excitation of the source. An association between the energy of ejected light charged particles and the extracted emission time scale has also been observed at intermediate energies [26–28]. Recent evidence [24] indicates that fragment emission does occur on a time scale commensurate with changes in the source characteristics. This result is based on the association between the strength of the fragment-fragment Coulomb interaction and the kinetic energy of the fragment pair. In the present paper we explore this association in greater detail. Specifically, we investigate the universality of this result (applicability to other systems) and the robustness of this signature of multifragmentation.

This paper is organized as follows: The experimental details are presented in Sec. II. General features of the reaction are described in Sec. III. In Sec. IV, inclusive velocity correlation functions are used to determine the spatial-temporal extent of the emitting system. The association between the spatial-temporal extent of the emitting system and the velocity of the fragment pair is explored in Sec. V. The universality of the trend and the effects of different selection criteria in velocity and angular range are also investigated in this section. In Sec. VI, we assess the uncertainties involved in measurement and in Sec. VII we examine the sensitivity of our results to trajectory model assumptions. Section VIII focuses on the effects of the rotational motion of the emitting system. The results of this work are summarized in Sec. IX.

II. EXPERIMENTAL DETAILS

The experiment was performed at the National Superconducting Cyclotron Laboratory at Michigan State University

*Present address: CRL, Chalk River, Ontario, Canada K0J 1J0.
†Present address: IUCF, Indiana University, Bloomington, Indiana 47408.
‡Present address: GSI, D-64220, Darmstadt, Germany.
§Present address: Deloitte and Touche, LLP, Two Word Financial Center, New York, New York 10281.
‖Present address: LBNL, University of California, Berkeley, California 94720.
¶Present address: Department of Chemistry, Hope College, Holland, Michigan 49423.
**Present address: Department of Physics, MIT, Cambridge, Massachusetts 02139.

(MSU) [29]. Beams of ^{84}Kr accelerated by the K1200 cyclotron to $E/A = 35$, 55, and 70 MeV were extracted with beam intensities of $1–2\times10^{8}$ particles per second and were focused onto self-supporting ^{197}Au targets. The target thickness was 1.3 mg/cm^2 for the experiments at $E/A = 35$ and 55 MeV and 4 mg/cm^2 at $E/A = 70$ MeV. Charged particles emitted in the angular range $5.4° \leqslant \theta_{lab} \leqslant 160°$ were detected with the combined MSU Miniball/Washington University Miniwall 4π phoswich detector array [30]. This detector system consisted of 268 low-threshold plastic-scintillator-CsI(Tl) phoswhich detectors mounted in 14 independent rings coaxial about the beam axis. The total geometric efficiency of these detectors is $\approx$ 90% of 4π.

Detectors in the Miniwall, which covered the angular range $5.4° \leqslant \theta_{lab} \leqslant 25°$, consisted of 80 μm thick plastic scintillator foils in front of 3 cm thick CsI(Tl) crystals. The energy thresholds for these detectors were $E_{th}/A \approx 4$ MeV (6 MeV) for $Z = 3$ ($Z = 10$) particles, respectively. Laboratory angles from $\theta_{lab} = 25°$ to 160° were covered by Miniball detectors which consisted of 40 μm plastic scintillator foils in front of 2 cm thick CsI(Tl) crystals. The thresholds for these detectors were $E_{th}/A \approx 2$ MeV (4 MeV) for $Z = 3$ ($Z = 10$) particles, respectively. Hardware discriminator thresholds of 5 MeV and 10 MeV were imposed on the $Z = 1$ particles for the Miniball and Miniwall, respectively, to avoid triggering on low energy electrons. Double hits consisting of a light charged particle ($Z \leqslant 2$) and an intermediate mass fragment (IMF, $3 \leqslant Z \leqslant 20$) or of two IMF's were identified as a single IMF. Double hits consisting of two light charged particles were identified as a single light charged particle. Multiple hits were estimated to reduce the charged particle multiplicity and the IMF multiplicity by 15–25 % and 1.5–2.5 %, respectively, depending on incident energy.

For each of the rings $\theta_{lab} \geqslant 25°$, a single Miniball detector was replaced with an ion chamber telescope [31]. These telescopes consisted of an axial field ion chamber operated at 30 torr of CF_4, a 500 μm thick passivated Si detector, and a 3 cm thick CsI(Tl) crystal, read out by a photodiode. The corresponding thresholds for particle identification were $E_{th}/A \approx 0.8$ MeV for $Z \leqslant 20$. These detectors provided reference single particle distributions for comparison to the distributions measured by the Miniball/Miniwall 4π array, particularly near threshold.

III. GENERAL REACTION CHARACTERISTICS

In order to preferentially select the most highly excited systems where multifragment decay describes the average behavior of the system [29], we have focused on central collisions. We have constructed a reduced impact parameter scale from the charged particle multiplicity following a geometrical prescription [32]. The central collisions included in this analysis have impact parameters of $b/b_{max} \leqslant 0.2$, where b_{max} refers to the maximum interaction radius for which two charged particles are emitted. The corresponding charged particle multiplicities for these central collisions are $N_c \geqslant 24$, 33, and 38 and the average multiplicity of IMF's, $\langle N_{IMF} \rangle \approx$ 4, 5, and 6 at $E/A = 35$, 55, and 70 MeV, respectively [29].

One characterizing observable of multifragmenting systems is the element distribution of emitted particles. In high energy ($80 \leqslant E_p \leqslant 350$ GeV) proton-induced reactions, Z distributions have been measured which obey a power law with $\tau = 2.6$ [33]. At considerably lower bombarding energies ($200 \leqslant E_{lab} \leqslant 3600$ MeV) for the ^{3}He + ^{nat}Ag system, power-law fits to the Z distributions reach a constant value of $\tau = 2.1$ at energies above 1800 MeV [34]. For heavy-ion reactions, where initial compression of the nuclear system might induce a liquid-gas phase transition, τ values of ≈ 2.2 have been measured for the ^{40}Ar + ^{197}Au system at $E/A =$ 220 MeV [35]. All of the above measurements, however, represent inclusive measurements where the fragment emission is averaged over a wide range of impact parameters. In the present experiment, we have investigated the impact parameter-selected character of Z distributions of fragments emitted in multifragmenting nuclear systems.

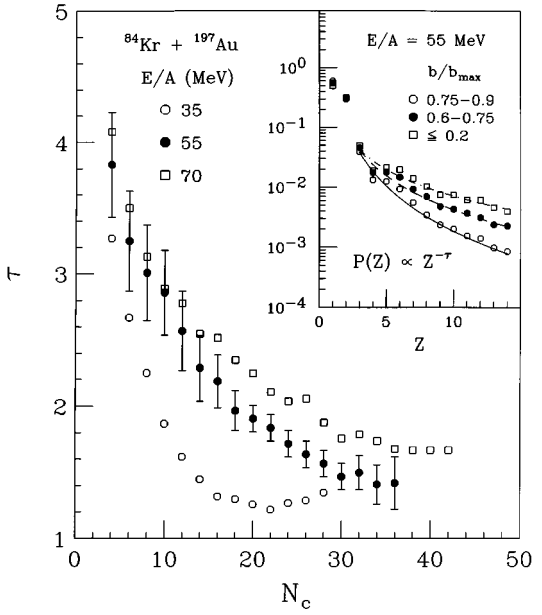

FIG. 1. Dependence of the fit parameter τ on N_c extracted from power law fits to the Z distributions measured in the angular range $25° \leqslant \theta_{lab} \leqslant 50°$ for the reaction ^{84}Kr + ^{197}Au at $E/A = 35$ (open circles), 55 (solid circles), and 70 MeV (open squares). Inset: Z distributions measured for particles emitted in collisions of different impact parameters at $E/A = 55$ MeV. The solid lines represent power law fits for $3 \leqslant Z \leqslant 14$ with the functional form $P(Z) \propto Z^{-\tau}$.

The change in the Z distributions of emitted particles with increasing charged particle multiplicity can be seen in Fig. 1. These distributions have been measured in the angular range $25° \leqslant \theta_{lab} \leqslant 50°$ using the low-threshold ionization chamber telescopes. We have fit the Z distributions for $3 \leqslant Z \leqslant 14$ with the functional form $P(Z) \propto Z^{-\tau}$. The dependence of the fit parameter τ on N_c at each of the different bombarding energies is plotted in Fig. 1. The inset in this figure depicts the Z distributions measured for particles emitted in collisions of different impact parameters in the reaction ^{84}Kr + ^{197}Au at $E/A = 55$ MeV, along with the power-law fits (solid lines). The distributions become less steep as we select on more central collisions.

The observed decrease in τ with increasing multiplicity can be understood in terms of the correlation between multiplicity and deposited energy. Fragment emission is expected to increase as the temperature of the emitted system is

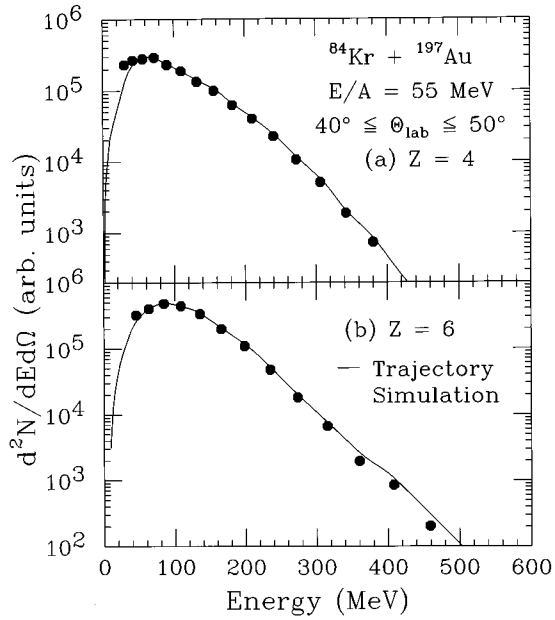

FIG. 2. (a) Fragment energy spectra for beryllium fragments emitted for central collisions in the reaction ^{84}Kr + ^{197}Au at E/A = 55 MeV. The solid line is the energy spectrum calculated by the three-body Coulomb trajectory model for Z_s=40, A_s=96, and R_s=7 fm. (b) The same as in panel (a) for carbon fragments.

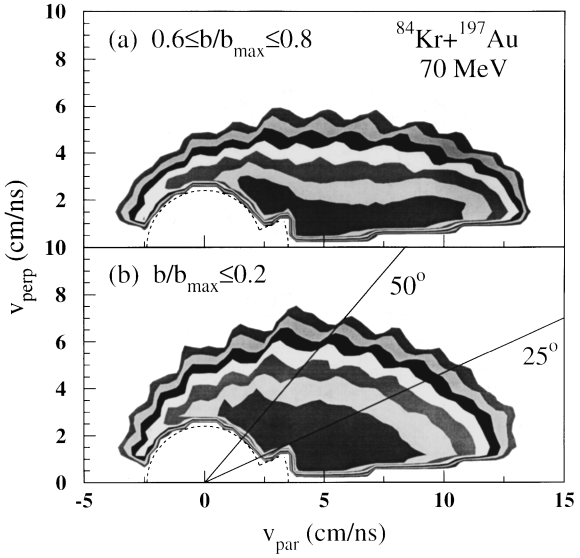

FIG. 3. (a) Velocity plots $d^2N/v^2dv\,d\Omega$ for beryllium fragments emitted in peripheral collisions for the reaction ^{84}Kr + ^{197}Au at E/A = 70 MeV. The detector thresholds are depicted as a dashed line. (b) The same as in panel (a) except for central collisions. The two solid lines indicate the angular region $25° \leqslant \theta_{lab} \leqslant 50°$.

raised and the Coulomb barrier effects are reduced [36]. The minimum τ achieved in central collisions increases from 1.2 at E/A = 35 MeV to 1.7 at E/A = 70 MeV. This increase in τ_{min} is qualitatively consistent either with a more excited system at E/A = 70 MeV fragmenting into smaller (on average) pieces or the increasing importance of sequential decay of excited primary fragments.

The details of the shape of the fragment kinetic energy spectra can provide useful information regarding the excitation and density of the emitting system [21]. The kinetic energy spectra for beryllium and carbon fragments emitted in central collisions in the reaction ^{84}Kr + ^{197}Au at E/A = 55 MeV are presented in Fig. 2. The spectra have been measured in the angular range $40° \leqslant \theta_{lab} \leqslant 50°$ using the Miniball detector array. The spectral shapes shown agree with the energy spectra measured with the ion chamber telescopes. At a given angle, these spectra can be represented as general Maxwell-Boltzmann distributions consisting of a single temperature, Coulomb barrier, and source velocity. However, the energy-angle distributions are not understandable in terms of the isotropic emission from a single equilibrium source because the angular distributions are anisotropic in any single rest frame.

The presence of multiple sources can clearly be seen in the velocity plots presented in Fig. 3. Beryllium fragments emitted in peripheral (b/b_{max} = 0.6–0.8) and central ($b/b_{max} \leqslant$ 0.2) collisions for E/A = 70 MeV are displayed in panels (a) and (b), respectively. The detector thresholds are indicated by the dashed lines. Peripheral interactions manifest a fragment velocity distribution with more than one component. The higher longitudinal velocity component is a broad distribution populating v_{par} between 4 and 11 cm/ns. This component might arise from projectile breakup reactions or emission from the excited projectilelike fragment following a dissipative binary collision. The second source of fragments in peripheral collisions is a targetlike source with a velocity $v_{par} \approx$ 1 cm/ns. For central collisions [panel (b)], the presence of two components is less obvious. It is clear that isotropic emission from a single equilibrated source of fixed velocity is inconsistent with the observed emission pattern. In order to minimize the effects of multiple sources, we have restricted the following analysis to the angular range $25° \leqslant \theta_{lab} \leqslant 50°$ [depicted as solid lines in panel (b)].

IV. INCLUSIVE CORRELATION FUNCTIONS

To examine the spatial-temporal size of the emitting source we have utilized two-fragment velocity correlations [36–44]. In previous work we have examined the decrease in the spatial-temporal extent of the source as the incident energy is increased [38,39]. This decrease in spatial-temporal extent is understandable if, by increasing the incident energy, systems of increased excitation are produced. Other studies indicate that, for a given system, the spatial-temporal extent decreases with increasing incident energy and then saturates at a minimum value [42]. Such a saturation might indicate either a saturation in energy deposition or the minimum spatial extent of the fragmenting source, consistent with an instantaneous breakup scenario. Distinguishing between these two possibilities is key to improving our understanding of multifragmenting nuclear systems.

The velocity correlation function $R(v_{red})$ is constructed by relating the coincidence yield Y to the background yield $Y^{\dagger}$:

$$\Sigma Y(\mathbf{v}_1,\mathbf{v}_2) = C^{\dagger}[1+R(v_{red})]\Sigma Y^{\dagger}(\mathbf{v}_1,\mathbf{v}_2),$$

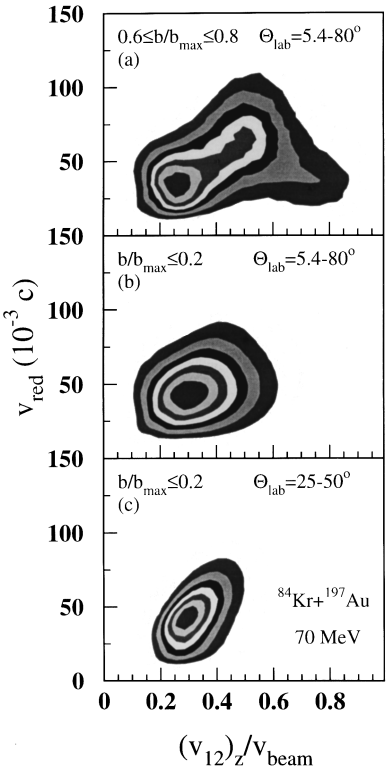

FIG. 4. (a) Dependence of the reduced velocity on the longitudinal component of the center-of-mass velocity of the IMF pair for peripheral collisions in the reaction ^{84}Kr + ^{197}Au at E/A = 70 MeV. (b) The same as in panel (a) except for central collisions. (c) The same as in panel (b) for the angular range $25° \leqslant \theta_{\rm lab} \leqslant 50°$.

where $\mathbf{v}_1$ and $\mathbf{v}_2$ are the laboratory velocities of the fragments, $v_{\rm red}$ is the reduced velocity given by $v_{\rm red}=(\mathbf{v}_1-\mathbf{v}_2)/(Z_1+Z_2)^{1/2}$ cm/ns [36], and $C^{\dagger}$ is the normalization constant determined by the requirement that $R(v_{\rm red})\rightarrow 0$ at large reduced relative velocities where the Coulomb repulsion is small. The background yield was constructed by selecting fragments from different events [45].

In order to understand the source of the IMF pairs, we have examined the dependence of the reduced velocity of the fragment pair, $v_{\rm red}$, on the longitudinal component of the center-of-mass velocity of the fragment pair divided by the beam velocity, $(v_{12})_z/v_{\rm beam}$. The results for $4\leqslant Z_1, Z_2 \leqslant 9$ in the angular range $5.4° \leqslant \theta_{\rm lab} \leqslant 80°$ are displayed in Fig. 4. The fragment mass is assumed to be the mass of the betastable isotope for that element. For peripheral interactions [panel (a)], three groups of IMF pairs can be distinguished. The first group, centered at $(v_{12})_z/v_{\rm beam}\approx$ 0.75 and $v_{\rm red}\approx 0.035c$, consists of pairs emitted from the projectilelike source. In the second group, centered at $(v_{12})_z/v_{\rm beam}\approx 0.25$ and $v_{\rm red}\approx 0.035c$, the pairs originate from the targetlike source. The third group, centered at $(v_{12})_z/v_{\rm beam}\approx 0.5$ and $v_{\rm red}\approx 0.065c$, is composed of events where one IMF is emitted from the projectilelike source and the second is emitted from the targetlike source. Fragments emitted in central collisions [panel (b)] originate predominantly from a single group, centered at $(v_{12})_z/v_{\rm beam}\approx 0.3$ and $v_{\rm red}\approx 0.050c$. The effect of limiting the angular range to $25° \leqslant \theta_{\rm lab} \leqslant 50°$ can be seen in panel (c). Selecting only pairs emitted in central collisions appears to preferentially isolate a single source. Similar results have previously been observed for the system ^{36}Ar + ^{197}Au [39].

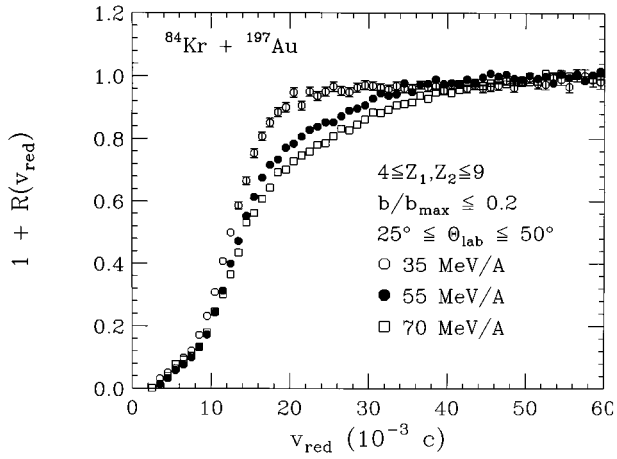

FIG. 5. Fragment-fragment velocity correlation functions for central collisions in the reaction ^{84}Kr + ^{197}Au at E/A = 35 (open circles), 55 (solid circles), and 70 MeV (open squares).

Velocity correlation functions for central collisions in the reaction ^{84}Kr + ^{197}Au at E/A = 35, 55, and 70 MeV are presented in Fig. 5. The fragments used in constructing the correlation functions include Z=4–9 emitted in the angular range $25° \leqslant \theta_{\rm lab} \leqslant 50°$. The normalization constant was determined in the region 0.05c to 0.08c where the correlation function is relatively flat. At low relative velocity, the mutual Coulomb repulsion between the fragments results in strong suppression in the probability of observing fragments of similar velocity. A more significant change in the shape of the correlation function is observed between E/A = 35 and 55 than between E/A = 55 and 70.

To quantitatively extract the spatial-temporal extent of the emitting system, we have performed simulations using a classical three-body Coulomb trajectory calculation [39]. This three-body trajectory model assumes the two fragments are emitted sequentially from the surface of a nucleus of initial atomic number Z_s, mass number A_s, and radius R_s, with the initial separation between source and IMF given by $R_s+R_{\rm IMF}$. The experimentally measured energy, angular, and Z distributions were used as inputs to the calculation. At E/A = 35 and 70 MeV, the source charge was assumed to be 57 and 32, respectively. This assumption was based upon the total measured charge (corrected for detector acceptance) and assuming the fragments are emitted last in the deexcitation cascade. Thus, this assumption represents an estimated lower limit for the source charge. The source velocities were determined from moving source fits to be 2.4 and 3 cm/ns at E/A = 35 and 70 MeV, respectively. The time between emissions was assumed to follow an exponential $\exp(-t/\tau)$ characterized by the mean emission time, τ.

The experimental energy spectra from the reaction ^{84}Kr + ^{197}Au at E/A = 55 MeV are compared to the energy spectra calculated by the three-body Coulomb trajectory model in Fig. 2. Reasonable agreement is found for the following assumptions: Z_s=40, A_s=96, R_s=7 fm, and τ = 100 fm/c. The source charge was chosen using the prescription as at the other two incident energies. The calculated energy spectra are fairly insensitive to the mean emission time. Cal-

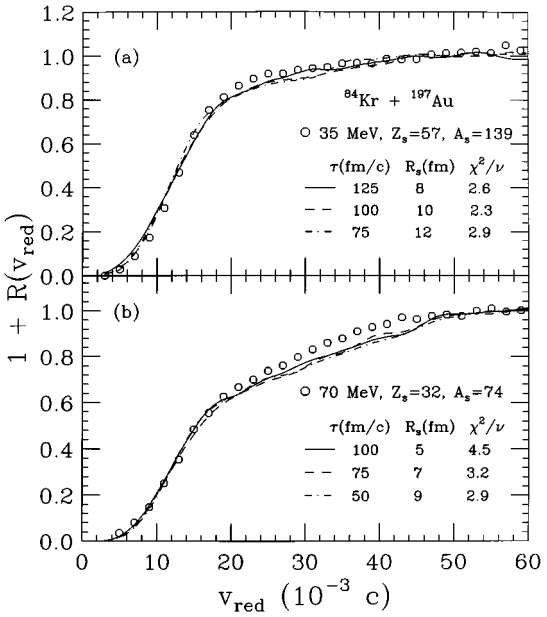

FIG. 6. (a) Comparisons of three-body trajectory calculations with the best χ^2/ν values to the experimental correlation functions for central collisions in the reaction ^{84}Kr + ^{197}Au at E/A = 35 MeV. (b) The same as in panel (a) except for E/A = 70 MeV.

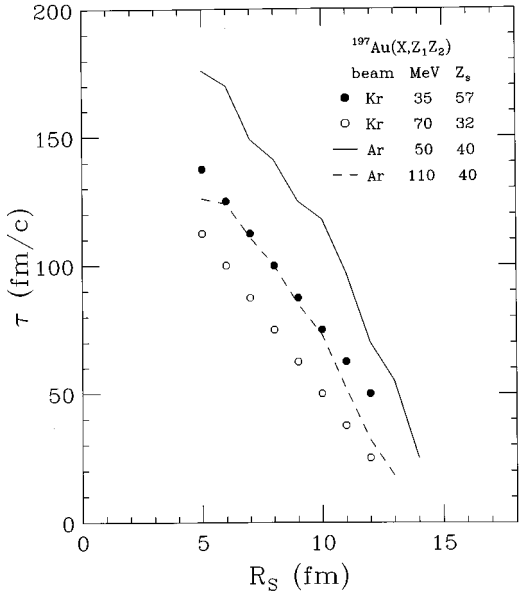

FIG. 7. Dependence of the mean emission time τ on the source radius R_s from comparisons with the best χ^2/ν between the three-body trajectory calculations and the experimental data. The solid and open circles represent central collisions in the reaction ^{84}Kr + ^{197}Au at E/A = 35 and 70 MeV, respectively. The solid and dashed lines represent central collisions in the reaction ^{36}Ar + ^{197}Au at E/A = 50 and 110 MeV, respectively.

culations using a larger source (e.g., Z_s = 79) fail to reproduce the low energy portion of the spectrum which suggests that a small source size is more appropriate for the simulations [39]. Because the trajectory model does not treat subbarrier emission, the correlation functions were constructed for fragments with a velocity above the trajectory model Coulomb barrier ($v \geq$ 4 cm/ns).

In Fig. 6, we display the fragment-fragment velocity correlation functions at E/A = 35 and 70 MeV together with the reference three-body trajectory calculations. For each value of source radius, the mean emission time is the best fit of the three-body calculation to the data, as determined by minimizing the χ^2 per degree of freedom, χ^2/ν [39]. If we assume a constant source radius, the mean emission time decreases with increasing bombarding energy. A more complete description of the spatial-temporal size of the emitting system is shown in Fig. 7. In these calculations, the variables R and τ have been treated as free parameters within physical limits. The lower limit on the radius of 5 fm is approximately equal to the sum of the radii for two IMF's. The upper limit of 12 fm corresponds to a source density of ρ/ρ_0 = 0.1. The solid and open circles represent best fits to the data at E/A = 35 (Z_s=57, A_s=139) and 70 MeV (Z_s=32, A_s=74), respectively. For the range of assumed source radius, $\tau \leq$ 140 fm/c for the data at E/A = 35 MeV and $\tau \leq$ 115 for the data at E/A = 70 MeV. These values represent the maximum mean emission times deduced at each bombarding energy.

Also shown in Fig. 7 for reference is the deduced spatial-temporal extent for the system ^{36}Ar + ^{197}Au [39] at E/A = 50 and 110 MeV. The 50 MeV and 110 MeV data are represented by the solid and dashed lines, respectively. In the Ar-induced reactions, a source charge of Z_s = 40 was assumed for the simulations to represent the limiting case where the light charged particles are emitted early in the deexcitation process, followed by the fragments. The spatial-temporal extent for the ^{36}Ar + ^{197}Au data at E/A = 110 is very similar to that of the ^{84}Kr + ^{197}Au data at E/A = 35 MeV, while the Ar data at E/A = 50 MeV have a larger spatial-temporal extent. A qualitative relationship is observed between increasing available energy and emitting source size. The available center-of-mass energies (assuming full linear momentum transfer) are 1522 and 3348 MeV for the ^{36}Ar + ^{197}Au system at E/A = 50 and 110 MeV and 2061 and 4122 MeV for the ^{84}Kr + ^{197}Au system at E/A = 35 and 70 MeV. The Kr data at E/A = 70 MeV have the largest available center-of-mass energy of the systems shown and the smallest spatial-temporal extent. This qualitative relationship between the maximum available energy and the source spatial-temporal extent suggests the underlying relationship between emission time and excitation. This connection between mean emission time and excitation is pursued further in the following section.

V. EXCLUSIVE CORRELATION FUNCTIONS

A recent investigation [24] has demonstrated the association between the strength of the fragment-fragment interaction and the minimum velocity of the fragment pair, defined as the velocity of the less energetic fragment. The width of the correlation function increases with increasing minimum velocity of the pair, signaling a decrease in the spatial-temporal extent of the emitting source. In this section, we examine the universality of this experimental trend and the effect of different selection criteria in velocity and angular range.

In Fig. 8(a) we present correlation functions constructed for fragment pairs $4 \leq Z_1, Z_2 \leq 9$ emitted in the angular range

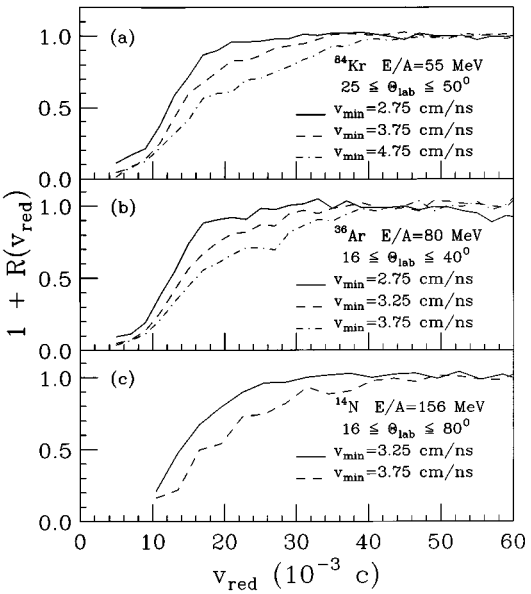

FIG. 8. (a) Experimental correlation functions for different cuts in the minimum velocity of the fragment pair associated with central collisions in the reaction ^{84}Kr + ^{197}Au at $E/A = 55$ MeV. (b) Exclusive experimental correlation functions for central collisions in the reaction ^{36}Ar + ^{197}Au at $E/A = 80$ MeV. (b) Exclusive experimental correlation functions for central collisions in the reaction ^{14}N + ^{197}Au at $E/A = 156$ MeV.

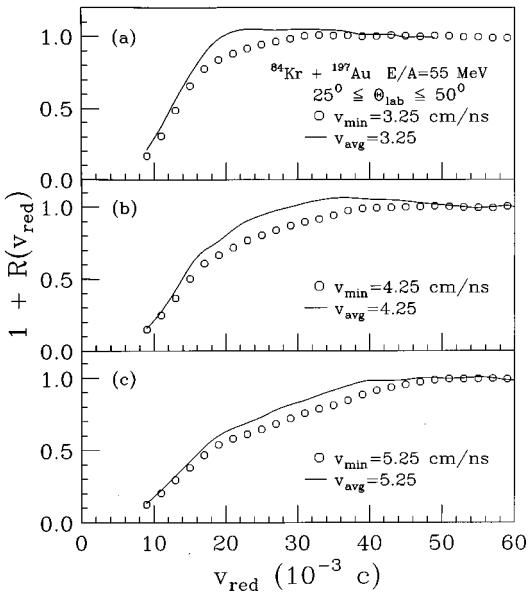

FIG. 9. (a) Correlation functions for $v_{\min} = 3.25$ cm/ns (open circles), and $v_{\text{avg}} = 3.25$ cm/ns (solid line), for central collisions in the reaction ^{84}Kr + ^{197}Au at $E/A = 55$ MeV. (b) The same as in panel (a) except $v_{\min}$, $v_{\text{avg}} = 4.25$ cm/ns. (c) The same as in panel (a) except $v_{\min}$, $v_{\text{avg}} = 5.25$ cm/ns.

$25° \leqslant \theta_{\text{lab}} \leqslant 50°$ in the reaction ^{84}Kr + ^{197}Au at $E/A = 55$ MeV. The correlation functions are shown with different cuts in minimum velocity $v_{\min}$. A significant increase in the width of the Coulomb hole with increasing minimum velocity is observed. In Fig. 8(b), correlation functions for different cuts in $v_{\min}$ are presented for the system ^{36}Ar + ^{197}Au at $E/A = 80$ MeV [39]. In this case, the correlation functions were constructed for fragments emitted in the angular range $16° \leqslant \theta_{\text{lab}} \leqslant 40°$. The increase in the width of the Coulomb hole with increasing minimum velocity is also observed for this system. We have also analyzed the ^{14}N + ^{197}Au at $E/A = 156$ MeV and constructed correlation functions in the angular range $16° \leqslant \theta_{\text{lab}} \leqslant 80°$. For this reaction, fragments pairs $4 \leqslant Z_1, Z_2 \leqslant 7$ were used to construct the correlation function since the cross section for $Z \geqslant 8$ is significantly reduced. As can be see in Fig. 8(c), increasing $v_{\min}$ also results in an increasing width of the Coulomb hole for this reaction. Since the characteristics of the fragment velocity spectra depend on the source size, velocity, and excitation of the system, different systems exhibit different velocity spectra. Consequently, to compare the different systems, we have chosen minimum velocity cuts based on certain fractions of the velocity distribution at each bombarding energy. For the Kr and Ar systems, the cuts correspond to the upper 90%, 70%, and 50% of the integrated velocity spectrum in the angular range over which the correlation function is constructed. For the N system, the cuts correspond to the upper 98% and 84% of the integrated velocity spectrum.

Selecting on the average velocity of the two fragments, $v_{\text{avg}} = (|v_1| + |v_2|)/2$, instead of $v_{\min}$ qualitatively produces the same result, as can be seen in Fig. 9. The two fragments in a given v_{avg} bin are chosen to have the same velocity within 1 cm/ns. Because selecting on $v_{\min}$ does not constrain the velocity of the more energetic fragment, cuts in $v_{\min}$ correspond on average to more energetic pairs and thus produce a slightly wider Coulomb hole than similar cuts in v_{avg}. One drawback of using v_{avg} is the limitation of a well-defined normalization region. Fragments of a certain v_{avg} have a maximum allowed relative velocity. Since the normalization region arises from particles with large v_{red}, selecting events with a small v_{avg} limits the normalization region.

Recent evidence [46] indicates that fragments of different atomic numbers might sample different time windows of the source deexcitation. Such an effect would distort the association between fragment velocity and emission time that we are currently investigating. To preclude this possibility, we have constructed correlation functions for pairs of boron fragments. The results are presented in Fig. 10. Correlation functions for different cuts in minimum velocity are shown in panel (a). An increase in the width of the Coulomb hole with increasing minimum velocity of the pair is clearly observed for the fragments where $Z_1 = Z_2 = 5$. In panels (b) and (c), we compare these results to simulations using the trajectory model described above. For the assumed source radius $R_s = 7$ fm, the mean emission time decreases from $\tau = 100$ to 0 fm/c as the minimum velocity of the pair is increased from 5 to 7 cm/ns. These results indicate that the increase in the strength of the Coulomb interaction with increasing velocity of the pair is not due solely to different Z_1, Z_2 combinations sampling different portions of the deexcitation cascade.

To examine the increase in the width of the correlation function quantitatively, we have extracted the half width at half maximum (HWHM), the width of the correlation function at half the asymptotic value. The dependence of the extracted HWHM values on the minimum velocity of the fragment pair for the two systems in the laboratory is shown

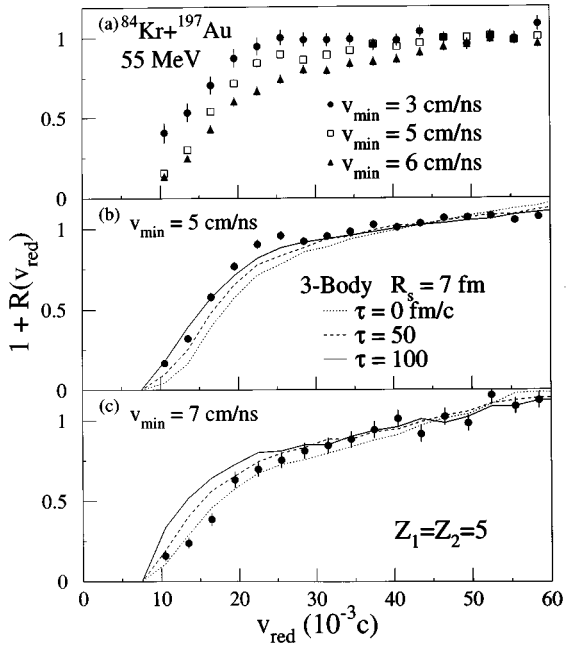

FIG. 10. (a) Correlation functions selected on the minimum velocity of the fragment pair for boron fragments emitted for central collisions in the reaction ^{84}Kr + ^{197}Au at E/A = 55 MeV. (b) Comparison between the data selected on $v_{\min}$ = 5 cm/ns and three-body Coulomb trajectory calculations with R_s = 7 fm and τ = 0 (dotted line), 50 (dashed line), and 100 (solid line). (b) The same as in panel (a) except $v_{\min}$ = 7 cm/ns.

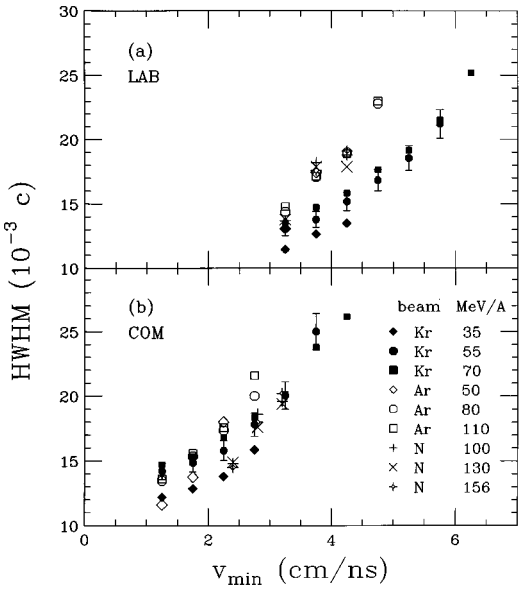

FIG. 11. (a) Dependence of the Coulomb interaction (HWHM) between fragments on the minimum fragment velocity in the laboratory frame. Central collisions in the reaction ^{84}Kr + ^{197}Au at E/A = 35, 55, and 70 MeV are represented by solid diamonds, circles, and squares. Central collisions in the reaction ^{36}Ar + ^{197}Au at E/A = 50, 80, and 110 MeV are represented by open diamonds, circles, and squares. Central collisions in the reaction ^{14}N + ^{197}Au at E/A = 100, 130, and 156 MeV are represented by vertical crosses, diagonal crosses, and fancy diamonds. (b) The same as in panel (a) except for the center-of-mass frame.

in Fig. 11(a). The data group themselves along two lines, one corresponding to the two more mass-asymmetric systems (N,Ar) and the other corresponding to the more mass-symmetric system (Kr). For a given minimum velocity in the Kr-induced reactions, the HWHM increases with increasing bombarding energy.

The two different lines observed for the N, Ar, and Kr systems in Fig. 11(a) might arise from the different kinematics of the three excitation functions. To minimize this trivial difference we have moved from the laboratory frame to the center-of-mass frame. An average source velocity was determined by fitting the experimental angular distribution. This source velocity corresponded to 1.0 cm/ns for all of the N-induced reactions; 2.6, 2.7, and 2.7 cm/ns for the Ar system at E/A = 50, 80, and 110 MeV; and 3.4, 3.9, and 4.0 cm/ns for the Kr system at E/A = 35, 55, and 70 MeV. The velocity cuts in the center-of-mass frame were chosen to correspond to the same fractions of the velocity distribution used in the laboratory frame. Removing the contribution of the source velocity reduces the distinct nature of the three projectile-target combinations [Fig. 11(b)].

Correlation functions gated on $v_{\min}$ are depicted in Fig. 12, both for the laboratory frame [panel (a)] and for the center of mass [panel (b)]. The increase in the HWHM in the angular range from 25° to 50° in the laboratory is similar to that observed in the range from 45° to 90° in the center of mass. This observation can be interpreted as the two ranges sampling comparable regions in phase space. The correlation functions for different cuts in minimum velocity for different angular ranges in the center of mass are presented in Fig. 13. The increase in the HWHM with increasing minimum velocity of the pair is greater at more backward angles in the center of mass. This result can perhaps be understood in the following context: The fragment cross section measured at forward angles contains a larger nonequilibrium contribution

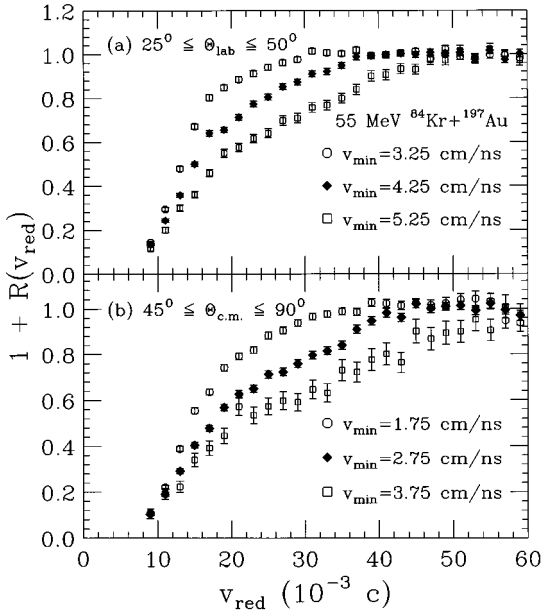

FIG. 12. (a) Correlation functions for different cuts in the minimum velocity of the fragment pair for fragments emitted in the angular range 25°≤θ_{lab}≤ 50° for central collisions in the reaction ^{84}Kr+ ^{197}Au at E/A = 55 MeV. (b) The same as in panel (a) except for fragments emitted in the angular range 45°≤$\theta_{c.m.}$≤ 90°.

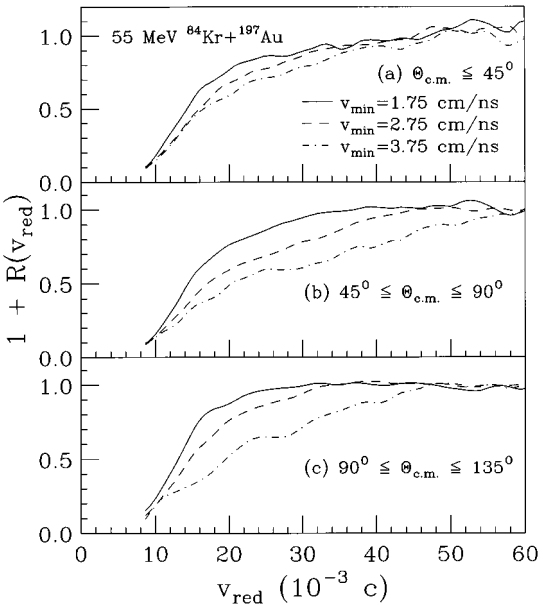

FIG. 13. Correlation functions for different cuts in the minimum fragment velocity for fragments emitted in the angular range $\theta_{c.m.} \leqslant 45°$ [panel (a)], $45° \leqslant \theta_{c.m.} \leqslant 90°$ [panel (b)], and $90° \leqslant \theta_{c.m.} \leqslant 135°$ [panel (c)].

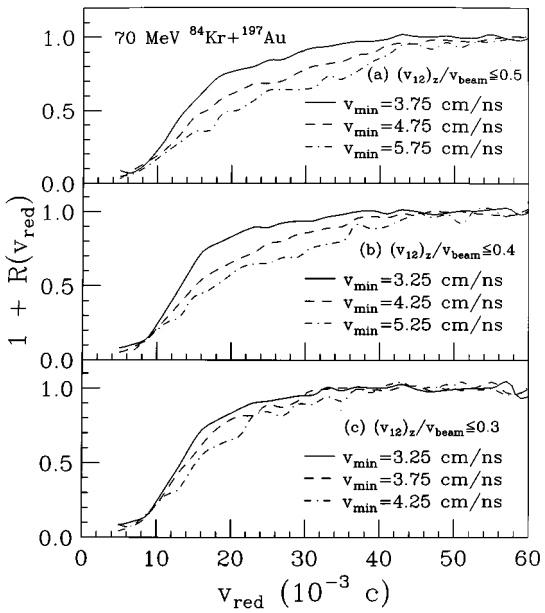

FIG. 15. Correlation functions for different cuts in the minimum fragment velocity for fragment pairs with $(v_{12})_z/v_{beam} \leqslant 0.5$ [panel (a)], $(v_{12})_z/v_{beam} \leqslant 0.4$ [panel (b)], and $(v_{12})_z/v_{beam} \leqslant 0.3$ [panel (c)].

than the fragment cross section at backward angles. This nonequilibrium component arises from fragment emission from sources associated with different amounts of linear momentum transfer and correspondingly different source velocities. Consequently, selection of fragment pairs of higher average velocity can select pairs from higher velocity sources, not necessarily sources of higher excitation.

In order to further isolate the contribution from different sources, we have performed an analysis in which we have restricted the longitudinal velocity of the IMF pair. Shown in Fig. 14 is the distribution of the longitudinal velocity, $(v_{12})_z/v_{beam}=(|v_1|_z+|v_2|_z)/v_{beam}$, for fragment pairs $4 \leqslant Z_1, Z_2 \leqslant 9$ emitted in the angular range $25° \leqslant \theta_{lab} \leqslant 50°$ for central collisions of the reaction ^{84}Kr + ^{197}Au at E/A = 70 MeV. The distribution is essentially a skewed

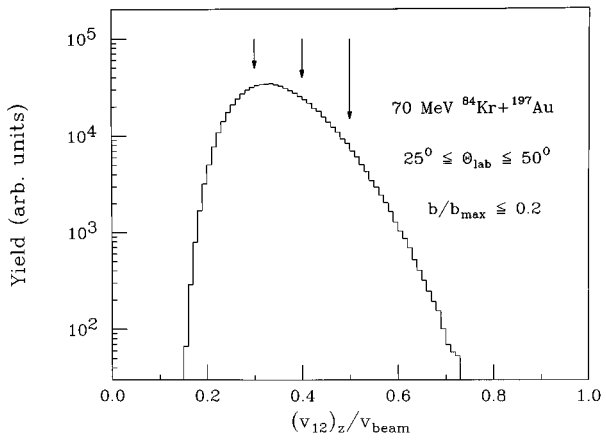

FIG. 14. Distribution of the longitudinal velocity of the IMF pair, $(v_{12})_z/v_{beam}$, for fragments emitted in the angular range $25° \leqslant \theta_{lab} \leqslant 50°$ for central collisions in the reaction ^{84}Kr + ^{197}Au at E/A = 70 MeV. The arrows correspond to values of $(v_{12})_z/v_{beam}$ = 0.3, 0.4, and 0.5.

Gaussian peaked at $(v_{12})_z/v_{beam}$ = 0.33 with an exponential tail extending to $(v_{12})_z/v_{beam} \approx 0.73$. Large values of $(v_{12})_z/v_{beam}$ correspond to fragment pairs of large longitudinal velocities, presumably from sources of high velocity. The arrows shown in the figure indicate values of $(v_{12})_z/v_{beam}$ = 0.3, 0.4, and 0.5.

We have constructed correlation functions in the same manner previously described with the additional restriction on $(v_{12})_z/v_{beam}$. Correlation functions shown in Fig. 15, panels (a), (b), and (c), correspond to restrictions of $(v_{12})_z/v_{beam} \leqslant$ 0.5, 0.4, and 0.3, respectively. As can be seen in the figure, in all cases increasing the v_{min} criterion results in an increasing width of the Coulomb hole indicating a stronger fragment-fragment interaction. Decreasing the threshold of $(v_{12})_z/v_{beam}$ from 0.5 to 0.3 limits the maximum v_{min} for which the correlation function can be constructed. The reduced change in the correlation functions shown in Fig. 15(c) as compared to Fig. 15(a) is due to this reduction in the v_{min} range.

The dependence of the extracted HWHM on v_{min} is shown in Fig. 16. The same dependence of HWHM on v_{min} is observed both for the $(v_{12})_z/v_{beam}$ integrated results, as well as the results from cases involving various restrictions in $(v_{12})_z/v_{beam}$. It is evident in Fig. 16 that the three cases involving restrictions in $(v_{12})_z/v_{beam}$ have (within the uncertainties shown) the same semiquantitative dependence of the HWHM on v_{min} as the $(v_{12})_z/v_{beam}$ integrated results. This insensitivity of the dependence of the HWHM on v_{min} to cuts in $(v_{12})_z/v_{beam}$ suggests that the dependence of the HWHM on v_{min} is not significantly attributable to fragments originating from sources with different longitudinal source velocities.

Recent analyses [44] have utilized directional cuts in the correlation function to attempt to resolve ambiguities be-

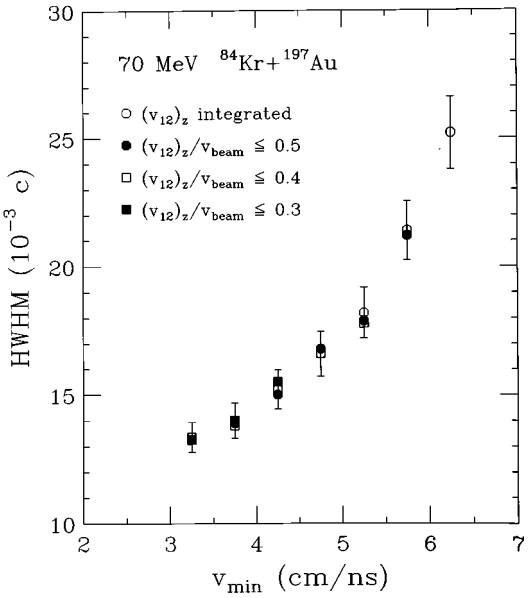

FIG. 16. Dependence of the Coulomb interaction (HWHM) between fragments on the minimum fragment velocity for fragment pairs with $(v_{12})_z/v_{\rm beam}$ integrated (open circles), $(v_{12})_z/v_{\rm beam} \leqslant 0.5$ (solid circles), $(v_{12})_z/v_{\rm beam} \leqslant 0.4$ (open squares), and $(v_{12})_z/v_{\rm beam} \leqslant 0.3$ (solid squares).

tween source size and lifetime. We have examined the effect of our velocity selection on such directionally constrained correlation functions. Transverse correlation functions with different cuts in minimum velocity for the system ^{84}Kr + ^{197}Au at $E/A = 70$ MeV are shown in Fig. 17. The transverse cut is defined as $\psi = 80°$–$90°$, where ψ is the angle between the reduced velocity $v_{\rm red}$ and the total velocity vector, $\mathbf{V} = \mathbf{v}_1 + \mathbf{v}_2$ [44]. The increase in the value of the HWHM with increasing minimum velocity of the fragment pair is semiquantitatively the same as previously displayed in Fig. 11. The longitudinal correlation functions ($\psi \leqslant 40°$, not shown) might exhibit a smaller increase in width with increasing $v_{\rm min}$. However, because of the lack of a well-defined normalization region, the extraction of the width of the correlation function is more difficult than for the transverse cut. Consequently, for the longitudinal cut, the quantitative dependence of the value of the HWHM on $v_{\rm min}$ is difficult to assess.

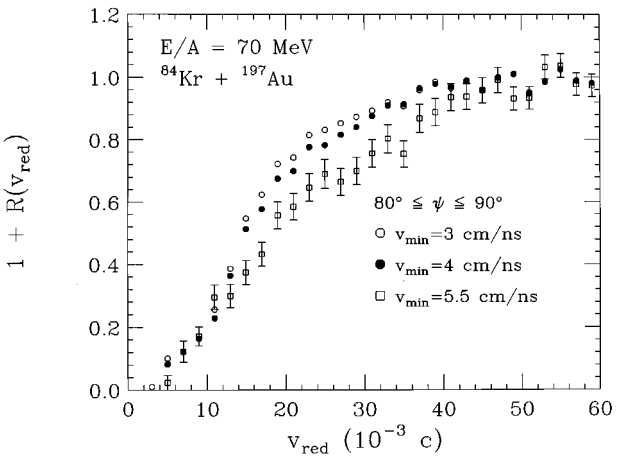

FIG. 17. Transverse correlation functions with restrictions on the minimum velocity of the fragment pair. The correlation functions were constructed from fragments emitted in the angular range $25° \leqslant \theta_{\rm lab} \leqslant 50°$ for central collisions in the reaction ^{84}Kr + ^{197}Au at $E/A = 70$ MeV.

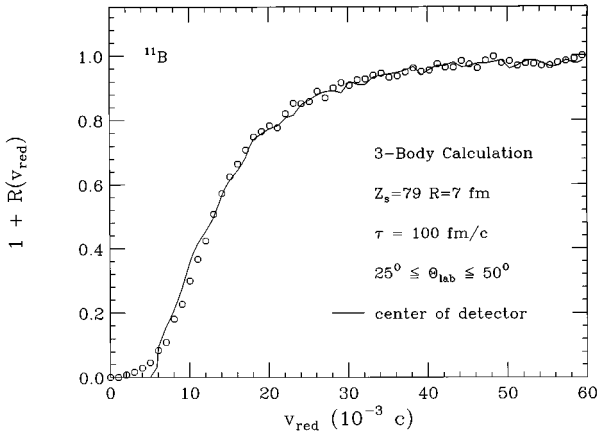

FIG. 18. Trajectory calculations for pairs of ^{11}B fragments, unfiltered (open circles) and filtered with the detector granularity (solid line).

VI. FINITE DETECTOR RESOLUTION EFFECTS

We now focus on the sensitivity of the observed trends to the detector granularity, energy resolution, and particle identification limitations of the detector setup. Determination of the magnitude of these effects allows us to assess the relative errors associated with the trends we have observed in the data.

The effect of finite angular resolution is illustrated in Fig. 18. The open circles depict the theoretical correlation function for ^{11}B fragments with a source of radius 7 fm and a mean emission time of 100 fm/c unfiltered by the detector granularity. The solid line is the result of filtering these results with the detector granularity. Because it is difficult to describe low energy emissions in the context of the classical trajectory calculation, the fragments have a minimum velocity cutoff of 4.5 cm/ns. As can be seen in the figure, the detector granularity produces only a minor distortion of the correlation function. The filtered correlation function is rotated about a point close to the HWHM, producing a wider Coulomb hole. This suggests that the ''true'' correlation function has a slightly narrower Coloumb hole than is measured by our apparatus; however, the quantity HWHM seems to be relatively insensitive to the rotation.

In Fig. 19(a) we examine the effect of the finite energy resolution of the experimental apparatus on the correlation function. The points are the correlation function constructed from the data measured with an estimated energy resolution of about 15% [29]. The solid and dashed lines are the result of smearing on a Gaussian distribution with a full width at half maximum (FWHM) of 10% and 20%, respectively. The 10% smearing does not produce a noticeable change in the correlation function, while the 20% case results in a small rotation, similar to that observed in the case of the detector granularity. Investigations of the energy spectra before and after the smearing have shown that the 20% FWHM smear-

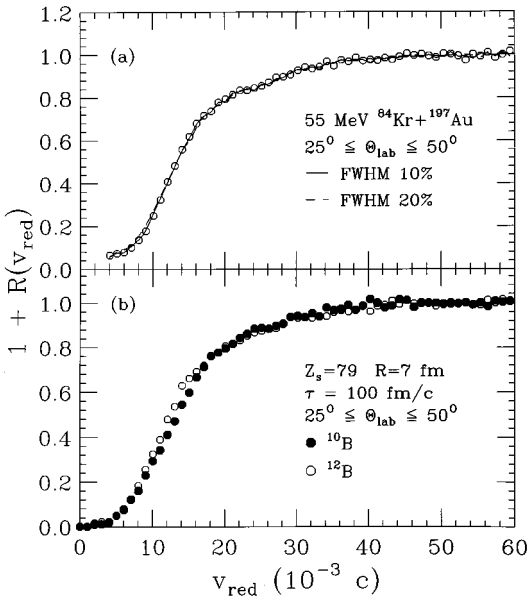

FIG. 19. (a) The correlation function for central collisions in the reaction ^{84}Kr + ^{197}Au at E/A = 55 MeV. The solid and dashed lines represent the results of smearing the experimentally measured energy distributions on a Gaussian distribution with a FWHM of 10% and 20%. (b) Trajectory calculations for pairs of ^{10}B (solid circles) and ^{12}B (open circles) fragments.

ing causes only a 1% change in the width, or second moment, of the Be energy spectrum measured in the range $25° \leqslant \theta_{lab} \leqslant 31°$.

Isotope misidentification of fragments is another source of uncertainty in this analysis. The theoretical correlation functions shown in Fig. 19(b) were constructed using the same conditions as in Fig. 18. We first assumed that all of the boron was $A=10$ (solid circles). Following this calculation we assumed all of the boron was $A=12$ (open circles). Increasing the mass of the boron fragment decreases the width of the Coulomb hole. For a given fragment energy, increasing the assigned mass decreases the resulting velocity. The corresponding decrease in relative velocity is reflected in the decreased width of the correlation function. To explicitly show the relationship between changes in the HWHM and the mean emission time with increasing fragment mass, we have performed simulations at fixed source radius for $\tau=25$, 50, and 100 fm/c. The results are plotted in Fig. 20. The difference in the HWHM between ^{10}B and ^{12}B corresponds to an uncertainty in mean emission time of about 25 fm/c. However, since these limits represent extreme cases regarding the mass distribution of boron fragments, 25 fm/c represents the upper limit for the uncertainty in the mean emission time due to mass misidentification.

VII. SENSITIVITY TO SOURCE ASSUMPTIONS

In order to extract more quantitative information regarding the emitting system, we have compared the experimental correlation functions with classical Coulomb three-body trajectory simulations. In these simulations it is necessary to make assumptions regarding the source characteristics (size, velocity, etc.). In this section, we examine the sensitivity of our deduced results to these assumptions.

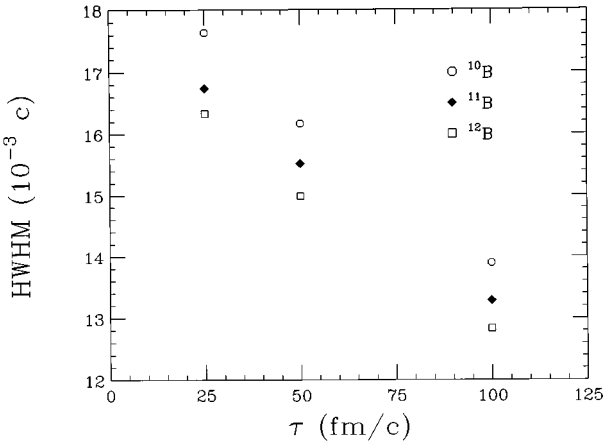

FIG. 20. Dependence of the width of the correlation function (HWHM) on the mean emission time for three-body Coulomb trajectory calculations for pairs of ^{10}B (open circles), ^{11}B (solid diamonds), and ^{12}B (open squares) fragments. The calculations were performed for Z_s = 79 (A_s = 197), R_s = 7 fm, and τ = 100 fm/c.

In Fig. 21 the extracted spatial-temporal extent of the emitting system in ^{84}Kr + ^{197}Au at E/A = 55 MeV/nucleon is depicted for different minimum velocity selection criteria. The correlation functions were constructed for pairs $4 \leqslant Z_1, Z_2 \leqslant 9$ emitted in the angular range 25°–50°. The simulations assumed a source charge of Z_s = 40, A_s = 96 (based on Z_{sum}) and a source velocity of 3 cm/ns. The symbols represent the best fits determined by minimizing the χ^2/ν. Minimum velocity gates of 4, 5, and 6 cm/ns are represented by open circles, solid circles, and open squares, respectively.

The increase in the Coulomb hole of the correlation func-

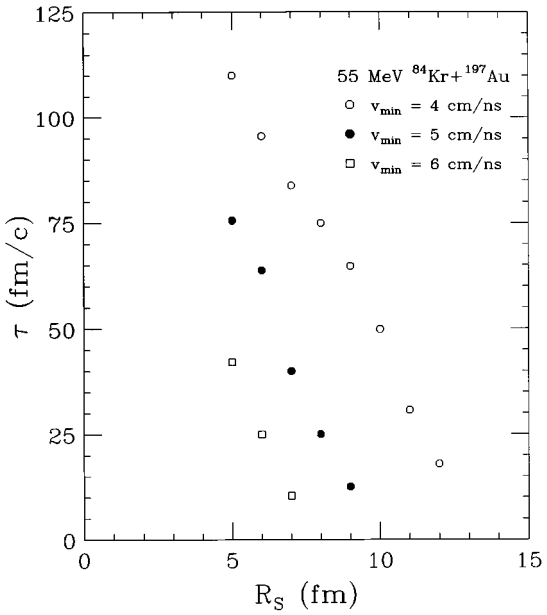

FIG. 21. Dependence of the mean emission time τ on the source radius R_s from comparisons for the best χ^2/ν between the three-body trajectory calculations and the experimental data. The open circles, solid circles, and open squares represent minimum velocity cutoffs of 4, 5, and 6 cm/ns.

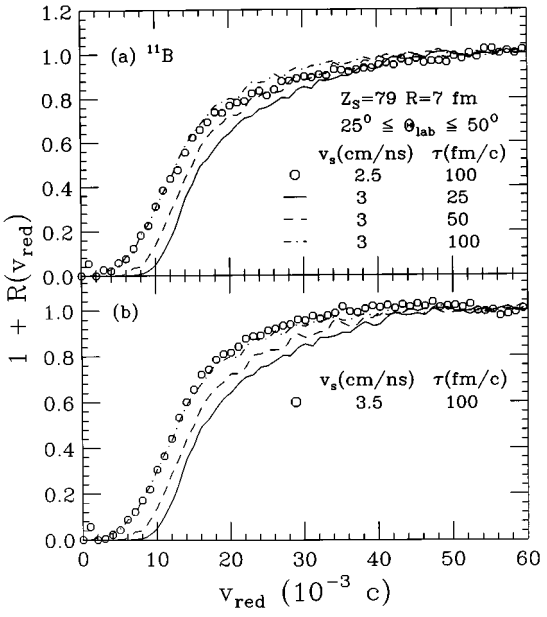

FIG. 22. (a) Trajectory calculations for ^{11}B fragments with v_s = 2.5 cm/ns and τ = 100 fm/c (open circles). The solid, dashed, and dot-dashed lines represent reference calculations with v_s = 3 cm/ns and τ = 25, 50, and 100 fm/c, respectively. (b) The same as in panel (a) except the open circles were calculated assuming v_s = 3.5 cm/ns.

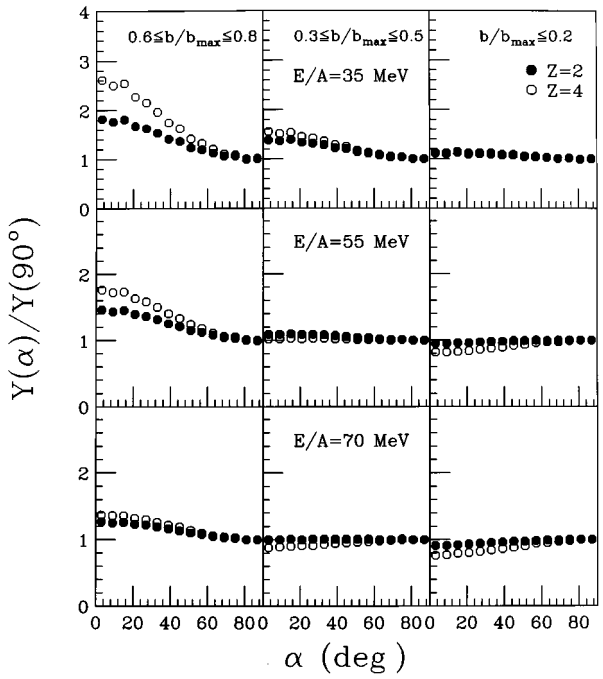

FIG. 23. Azimuthal distributions with respect to the reconstructed reaction plane for peripheral (b/b_{max}=0.6–0.8), midcentral (b/b_{max}=0.3–0.5), and central ($b/b_{max} \leq$ 0.2) collisions in the reaction ^{84}Kr + ^{197}Au at E/A = 35, 55, and 70 MeV. The solid and open circles represent alpha particles and beryllium fragments, respectively.

tion with an increasing cut on minimum velocity corresponds to a decrease in the spatial-temporal extent of the emitting system and can be reproduced in the simulation by a reduction of either the source radius R_s or the mean emission time τ. We have previously interpreted the dependence of the HWHM of the correlation function as a decrease in the mean emission time between fragments with increasing minimum velocity while the source radius remains constant. An equally valid scenario is a source of constant mean emission time that increases in size during the emission process. Such a scenario might be valid if fragment emission occurred early in the collision dynamics. The size of the source would increase as the energy deposition proceeded. As can be seen in Fig. 21, changing v_{min} from 4 cm/ns to 5 cm/ns can be viewed as either a decrease in mean emission time of 50 fm/c (R_s = 10 fm, τ = 50 fm/c $\rightarrow$ R_s = 10 fm, τ = 0 fm/c) or a decrease in source size of 3.5 fm/c (R_s = 10 fm, τ = 50 fm/c $\rightarrow$ R_s = 6.5 fm, τ = 50 fm/c).

We next examine the sensitivity of the correlation function to the assumed source velocity. The comparison has been carried out within the framework of the three-body trajectory calulation. In panels (a) and (b) of Fig. 22, the results of trajectory calculations for ^{11}B fragments assuming a source velocity of 2.5 and 3.5 cm/ns are shown as open circles. The assumed source charge is 79 (A_s=197) with a radius of 7 fm and mean emission time τ of 100 fm/c. To estimate the difference between these two calculations, reference simulations with v_s=3 cm/ns and mean emission times τ of 25, 50, and 100 fm/c are plotted as solid, dashed, and dot-dashed lines, respectively, in both panels.

In panel (a), the simulation with v_s = 2.5 cm/ns (open circles) has a Coulomb hole that is slightly wider than that for the reference simulation with τ=100 fm/c. The simulation with v_s=3.5 cm/ns in panel (b) is somewhat narrower than the 100 fm/c reference simulation, corresponding to a weaker interaction with increasing source velocity. For a radius of 7 fm, this corresponds to a change in mean emission time of significantly less than 25 fm/c. We have also examined the change in the HWHM. With the reference calculations as a rough scale, the change appears to be less than 10 fm/c for an increase in source velocity from 2.5 to 3.5 cm/ns.

VIII. ANGULAR MOMENTUM DISTORTIONS

Recent measurements have demonstrated the persistence of collective motion even for small impact parameters and that these collective effects impose distortions on fragment-fragment correlations [47–54]. Such effects must be accounted for when constructing correlation functions. To quantify rotational motion present in the ^{84}Kr + ^{197}Au system at the energies measured, we have constructed azimuthal distributions [49,50,52,53] and azimuthal correlation functions [47,48,50,51]. For the construction of the azimuthal distributions, the reaction plane was determined for each fragment using techniques previously described [49,53].

In Fig. 23 we present azimuthal distributions for peripheral (b/b_{max}=0.6–0.8), midcentral (b/b_{max}=0.3–0.5), and central ($b/b_{max} \leq$ 0.2) collisions at the three bombarding energies. The parameter α is defined as the azimuthal angle between the fragment velocity vector and the reaction plane. We have plotted the ratio of the yield for each value of α (normalized to unity at α=90°) for helium and beryllium fragments. A ratio larger than unity at α=0° reflects enhanced emission in the reaction plane. Since particle emission from a rotating source is enhanced in the plane, this

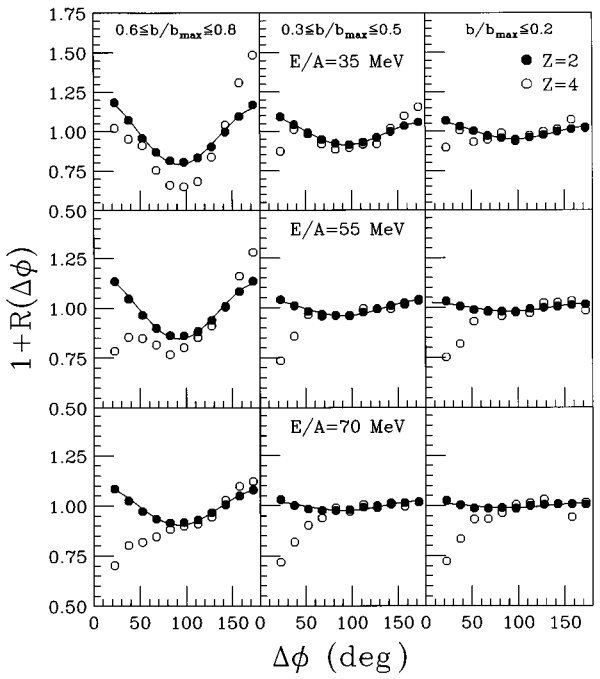

FIG. 24. Azimuthal correlation functions for peripheral (b/b_{max}=0.6–0.8), midcentral (b/b_{max}=0.3–0.5), and central ($b/b_{max} \leq$ 0.2) collisions in the reaction ^{84}Kr + ^{197}Au at E/A = 35, 55, and 70 MeV. The solid and open circles represent alpha particles and beryllium fragments, respectively. Fits to the alpha particle correlation functions with the form $A[1+\lambda_1\cos(\Delta\phi)+\lambda_2\cos(2\Delta\phi)]$ are displayed as solid lines.

ratio is a quantitative measure of the rotational motion of the emitting system.

In Fig. 23 beryllium fragments emitted in peripheral reactions at E/A = 35 MeV have the highest anisotropy: $Y(\alpha=0°)/Y(\alpha=90°)$ = 2.6. This ratio decreases to about 1.4 as the bombarding energy is increased to 70 MeV/nucleon. The helium particles have a lower anisotropy than the beryllium fragments, but this difference becomes less significant as the bombarding energy is increased. In comparison, azimuthal distributions constructed for midcentral collisions in the reaction ^{36}Ar + ^{197}Au at E/A = 35 MeV had $Y(0°)/Y(90°)$ ratios of 2.5 (4.5) for Z=2 (Z=4) particles [49].

For central collisions, the azimuthal distributions are essentially flat. The azimuthal distributions for beryllium fragments emitted in the central collisions have $Y(0°)/Y(90°)$ ratios that are less than 1. This suppression at small azimuthal angle is due to the higher Coulomb repulsion for particles emitted in the plane. Since all of the velocity correlation functions in this analysis were constructed for central collisions, the anisotropy distortions are expected to be small.

The results of an alternative method for investigating the angular momentum present in this reaction for various impact parameters are presented in Fig. 24. The azimuthal correlation function is defined [47] as

$$Y(\Delta\phi)/Y'(\Delta\phi)=C[1+R(\Delta\phi)],$$

where $Y(\Delta\phi)$ is the coincidence yield of two (identical) particles emitted with relative azimuthal angle $\Delta\phi$, $Y'(\Delta\phi)$ is the background yield constructed by mixing particle yields from different events which satisfy the same constraints as the coincidence yield, and C is a normalization constant. The correlation functions were constructed from fragments emitted in the polar angular range of 25°–50° in the laboratory and were normalized so that the average value is 1. Emission from a rotating source results in a characteristic V shape, i.e., suppression in the correlation function at $\Delta\phi$=90°.

TABLE I. Table of parameters for fits to the azimuthal correlation functions for ^{84}Kr + ^{197}Au at E/A = 35 MeV with the form $A[1+\lambda_1\cos(\Delta\phi)+\lambda_2\cos(2\Delta\phi)]$. The errors are estimated to be $\pm$0.10 for λ_1 and $\pm$0.05 for λ_2.

b/b_{max}	$\langle b/b_{max}\rangle$	Z=2		Z=4		Z=6	
		λ_1	λ_2	λ_1	λ_2	λ_1	λ_2
0.0–0.2	0.14	0.024	0.050	-0.27	-0.066	0.092	0.11
0.2–0.4	0.32	0.025	0.073	0.32	0.21	0.22	0.20
0.4–0.6	0.51	0.031	0.12	0.20	0.27	0.20	0.30
0.6–0.8	0.71	0.046	0.22	0.55	0.54	0.62	0.59
0.8–1.0	0.91	0.12	0.35	0.61	0.66	0.88	0.73

The same trends evident in Fig. 23 are apparent in Fig. 24 as well: The anisotropy decreases both with increasing beam energy and increasing centrality. The beryllium fragments exhibit more anisotropy than helium particles and are suppressed near $\Delta\phi$=0. Except for this Coulomb suppression, the azimuthal correlation functions are relatively flat for central collisions.

To quantitatively compare the azimuthal anisotropies, we have fit the azimuthal correlation functions with the form

$$A[1+\lambda_1\cos(\Delta\phi)+\lambda_2\cos(2\Delta\phi)],$$

where λ_1 and λ_2 are treated as free parameters [47,48] and A is a normalization constant. Positive (negative) values of λ_1 indicate preferential emission of the particle pair to the same side (opposite sides) of the beam (resonance effects, momentum conservation) and large λ_2 values may be associated with rotational collective motion of the emitting system [47]. For the IMF azimuthal correlation functions, we have performed the fits over the range $\Delta\phi$ = 90°–180°. The fits for alpha particles are depicted as solid lines in Fig. 24.

The largest values of λ_1 and λ_2 are observed at E/A = 35 MeV. The values are summarized in Table I. These values for Z=2 are comparable to those determined from alpha particles emitted in the reaction ^{36}Ar + ^{197}Au at E/A = 35, 50, 80, and 110 MeV where the values of λ_1 vary between ≈ -0.02 (central) to $\approx$ 0.13 (peripheral) and the values of λ_2 range between $\approx$ 0.02 (central) to $\approx$ 0.6 (peripheral) [47]. The values of λ_2 increase with increasing Z of the fragments, consistent with a larger sensitivity of heavy fragments to residual rotation in the emitting system. The values of λ_1 and λ_2 for beryllium and carbon fragments emitted in the reaction at E/A = 35 are also summarized in Table I. In the energy range being studied, both λ_1 and λ_2 decrease with increasing bombarding energy.

Figure 25 shows the small effect of correcting for the anisotropy in the reduced velocity correlation functions con-

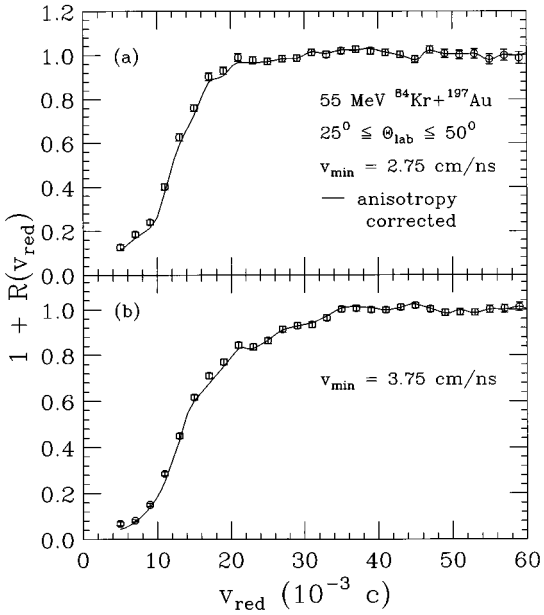

FIG. 25. (a) Correlation function for $v_{\min} = 2.75$ cm/ns for central collisions in the reaction ^{84}Kr + ^{197}Au at $E/A = 55$ MeV with (solid line) and without (open circles) the anisotropy correction (see text). (b) The same as in panel (a) except $v_{\min} = 3.75$ cm/ns.

structed for central collisions in the reaction ^{84}Kr + ^{197}Au at $E/A = 55$ MeV. The correlation functions shown were cut on minimum velocities of $v_{\min}$=2.75 and 3.75 cm/ns in panels (a) and (b), respectively. In the construction of the denominator, the events are rotated into a unique reaction plane [55]. A reaction plane is defined for each fragment. The reaction plane of the first fragment is then rotated in the azimuthal angle ϕ to coincide with the reaction plane of the second fragment. Distortions of the velocity correlation functions due to angular momentum of the emitting system are apparently negligible for central collisions. All correlation functions previously shown in Figs. 5–17 have been corrected for the azimuthal anisotropy.

IX. SUMMARY

Recent evidence [24] indicates an association between the strength of the fragment-fragment Coulomb interaction and the kinetic energy of the fragment pair. In the present paper we have investigated this association in greater detail. The increase in the width of the Coulomb hole with increasing velocity of the fragments was observed for cuts on the average velocity of the pair, for different angular regions in the center of mass, and for pairs where $Z_1 = Z_2$. Restrictions were also placed on the longitudinal velocity of the fragment pair in order to minimize the contribution from multiple sources. Even fragment pairs subjected to these more restrictive conditions exhibited the trend of higher velocity fragments being associated with a stronger fragment-fragment interaction. This trend was also observed in the systems ^{36}Ar + ^{197}Au at $E/A = 50$, 80, and 110 MeV and ^{14}N + ^{197}Au at $E/A = 100$, 130, and 156 MeV. We have examined the effects of detector granularity, energy resolution, and particle identification on the correlation function. We have also examined the sensitivity of our deduced results to assumptions about the source characteristics and to the rotational motion of the emitting source.

In conclusion, the association between the spatial-temporal extent of the emitting system and portions of the one-body energy spectrum is strong and the dependences much larger than the uncertainties in both the experimental measurements or trajectory calculations. Moreover, it appears to be a universal feature of multifragment decay attributable to the deexcitation of the source on a time scale concurrent with the fragment emission time scale.

ACKNOWLEDGMENTS

We would like to acknowledge the valuable assistance of the staff and operating personnel of the K1200 cyclotron at Michigan State University for providing the high quality beams which made this experiment possible. One of the authors (R.D.) gratefully acknowledges the support of the Sloan Foundation through the Alfred P. Sloan Fellowship program. This work was supported by the U.S. Department of Energy under Contracts No. DE-FG02-92ER-40714 (Indiana University) and No. DE-FG02-87ER-40316 (Washington University) and the National Science Foundation under Grants Nos. PHY-90-15255 and PHY-92-14992 (Michigan State University).

[1] W. Bauer *et al.*, Phys. Rev. Lett. **58**, 863 (1987).
[2] J. Aichelin *et al.*, Phys. Rev. C **37**, 2451 (1988).
[3] G. Peilert *et al.*, Phys. Rev. C **39**, 1402 (1989).
[4] D.H. Boal and J.J.N. Glosli, Phys. Rev. C **37**, 91 (1988).
[5] D.H.E. Gross *et al.*, Phys. Rev. Lett. **56**, 1544 (1986).
[6] J. Bondorf *et al.*, Nucl. Phys. **A444**, 460 (1985).
[7] L.G. Moretto *et al.*, Phys. Rev. Lett. **74**, 1530 (1995).
[8] W.A. Friedman and W.G. Lynch, Phys. Rev. C **28**, 16 (1983).
[9] W.A. Friedman and W.G. Lynch, Phys. Rev. C **28**, 950 (1983).
[10] W.A. Friedman, Phys. Rev. C **40**, 2055 (1989).
[11] W.A. Friedman, Phys. Rev. C **42**, 667 (1990).
[12] G. Bertsch and P.J. Siemens, Phys. Lett. **126B**, 9 (1983).
[13] G. Papp, Heavy Ion Physics (submitted).
[14] J. Randrup, Nucl. Phys. **A583**, 329 (1995).
[15] J.E. Finn *et al.*, Phys. Rev. Lett. **49**, 1321 (1982).
[16] J.W. Harris *et al.*, Nucl. Phys. **A471**, 241c (1987).
[17] C.A. Ogilvie *et al.*, Phys. Rev. Lett. **67**, 1214 (1991).
[18] R.T. de Souza *et al.*, Phys. Lett. B **268**, 6 (1991).
[19] D.R. Bowman *et al.*, Phys. Rev. Lett. **67**, 1527 (1991).
[20] R. Wada *et al.*, Phys. Rev. Lett. **58**, 1829 (1987).
[21] K. Kwiatkowski *et al.*, Phys. Rev. Lett. **74**, 3756 (1995).
[22] L. Phair *et al.*, Phys. Rev. Lett. **75**, 213 (1995).
[23] M.L. Gilkes *et al.*, Phys. Rev. Lett. **73**, 1590 (1994).
[24] E. Cornell *et al.*, Phys. Rev. Lett. **75**, 1475 (1995).

[25] C.O. Dorso and J. Aichelin, Phys. Lett. B **345**, 197 (1995).
[26] C.J. Gelderloos and John Alexander, Nucl. Instrum. Methods Phys. Res. A **349**, 618 (1994).
[27] C.J. Gelderloos *et al.*, Phys. Rev. Lett. **75**, 3082 (1995).
[28] C.J. Gelderloos *et al.*, Phys. Rev. C **52**, R2834 (1995).
[29] G.F. Peaslee *et al.*, Phys. Rev. C **49**, R2271 (1994).
[30] R.T. de Souza *et al.*, Nucl. Instrum. Methods Phys. Res. A **295**, 109 (1990).
[31] D. Fox *et al.*, Nucl. Instrum. Methods Phys. Res. A **368**, 709 (1996).
[32] C. Cavata *et al.*, Phys. Rev. C **42**, 1760 (1990).
[33] A.S. Hirsch *et al.*, Phys. Rev. C **29**, 508 (1984).
[34] S.J. Yennello *et al.*, Phys. Lett. B **246**, 26 (1990).
[35] U. Milkau *et al.*, Phys. Rev. C **44**, R1242 (1991).
[36] Y.D. Kim *et al.*, Phys. Rev. C **45**, 338 (1992).
[37] Y.D. Kim *et al.*, Phys. Rev. Lett. **67**, 14 (1991).
[38] D. Fox *et al.*, Phys. Rev. C **47**, R421 (1993).
[39] D. Fox *et al.*, Phys. Rev. C **50**, 2424 (1994).
[40] R. Trockel *et al.*, Phys. Rev. Lett. **59**, 2844 (1987).
[41] R. Bougault *et al.*, Phys. Lett. B **232**, 291 (1989).
[42] E. Bauge *et al.*, Phys. Rev. Lett. **70**, 3705 (1993).
[43] T.C. Sangster *et al.*, Phys. Rev. C **47**, R2457 (1993).
[44] T. Glasmacher *et al.*, Phys. Rev. C **50**, 952 (1994).
[45] M.A. Lisa, *et al.*, Phys. Rev. C **44**, 2865 (1991).
[46] E. Cornell (unpublished).
[47] L. Phair *et al.*, Nucl. Phys. **A564**, 453 (1993).
[48] R.A. Lacey *et al.*, Phys. Rev. Lett. **70**, 1224 (1993).
[49] M.B. Tsang *et al.*, Phys. Rev. C **44**, 2065 (1991).
[50] M.B. Tsang *et al.*, Phys. Rev. C **42**, R15 (1990).
[51] M.B. Tsang *et al.*, Phys. Lett. **148B**, 265 (1984).
[52] W.K. Wilson *et al.*, Phys. Rev. C **51**, 3136 (1995).
[53] W.K. Wilson *et al.*, Phys. Rev. C **41**, R1881 (1990).
[54] Y.G. Ma and W.Q. Shen, Phys. Rev. C **51**, 3256 (1995).
[55] B. Kämpfer *et al.*, Phys. Rev. C **48**, R955 (1993).